

Peculiarities of the Dynamics of Solar NOAA Active Region 12673

A. V. GETLING¹¹*Skobeltsyn Institute of Nuclear Physics, Lomonosov Moscow State University, Moscow, 119991 Russia*

ABSTRACT

The dynamics of active region (AR) 12673 is qualitatively studied using observational data obtained with the Helioseismic and Magnetic Imager of the *Solar Dynamics Observatory* on August 31–September 8, 2017. This AR was remarkable for its complex structure and extraordinary flare productivity. The sunspot group in this AR consisted of (1) an old, well-developed and highly stable, coherent sunspot, which had also been observed two solar rotations earlier, and (2) a rapidly developing cluster of umbral and penumbral fragments. Cluster (2) formed two elongated, arc-shaped chains of spot elements, skirting around the major sunspot (1), with two chains of magnetic elements spatially coinciding with the arcs. AR components (1) and (2) were in relative motion, cluster (2) overtaking spot (1), and their relative velocity agrees in order of magnitude with the velocity jump over the near-surface shear layer, or *leptocline*. The pattern of motion of the features about the main spot bears amazing resemblance to the pattern of a fluid flow about a roundish body. This suggests that spot (1) was dynamically coupled with the surface layers, while cluster (2) developed in deeper layers of the convection zone. The magnetic-flux emergence in cluster (2) appeared to be associated with fluid motions similar to roll convection. The mutual approach of components (1) and (2) gave rise to lights bridges in the umbrae of sunspots with the magnetic field having the same sign on both sides of the bridge.

Keywords: Sun: magnetic fields — Sun: photosphere — sunspots

1. INTRODUCTION

Solar NOAA active region (AR) 12673, which was observed in September 2017, was remarkable for its complex structure and extraordinary flare productivity—the highest in Solar Cycle 24 (Yang et al. 2017; Attie et al. 2018; Hou et al. 2018). It produced 4 flares above X1 class and 8 flares above M3 class; moreover, its X-9.3 (on 2017 September 6, 11:53 UT) flare was the most intense one since 2005 (see, e.g., Sun & Norton 2017). The behavior of the flow and magnetic field in this AR deserves particular attention. In particular, the magnetic-field and sunspot dynamics suggests that different parts of this complex aggregate might be dynamically coupled with different layers of the solar convection zone and atmosphere.

The sunspot group in AR 12673 consisted of (1) a well developed, highly stable, coherent sunspot with a magnetic field exceeding 2 kG, which had previously existed, and (2) a cluster of umbral and penumbral fragments, which emerged on 2017 September 2 and fused later into new larger spots. We will see that component (2) was not definitely opposite

to spot (1) in its polarity, so that the whole magnetic configuration of AR 12673 could not be classified as a bipolar one. Sunspot (1), as its position on the solar disk suggests, was already present two solar rotations before cluster (2) started developing (Figure 1a), being the leading spot of a regular bipolar group attributed to AR 12665. One rotation later, this sunspot appeared to be unipolar, belonging to AR 12670 (Figure 1b).

The evolution of AR 12673 (Figures 1c–1e) as the main subject of this study will be discussed below. Now, we only note that a unipolar sunspot was also present not far from the previous location of AR 12673 one and two rotations after the period of development of AR 12673, being attributed to ARs 12682 and 12685 (Figures 1f and 1g, respectively).

This study follows the avenue of investigation of the AR and sunspot-group formation mechanisms as outlined by Getling & Buchnev (2019) and based on parallel analyses of the magnetic and velocity fields simultaneously recorded at early AR-development stages. Currently available observational facilities provide a wealth of data admitting multifaceted description of the MHD processes under question. This should be highly promising in terms of comprehending the physical mechanisms involved.

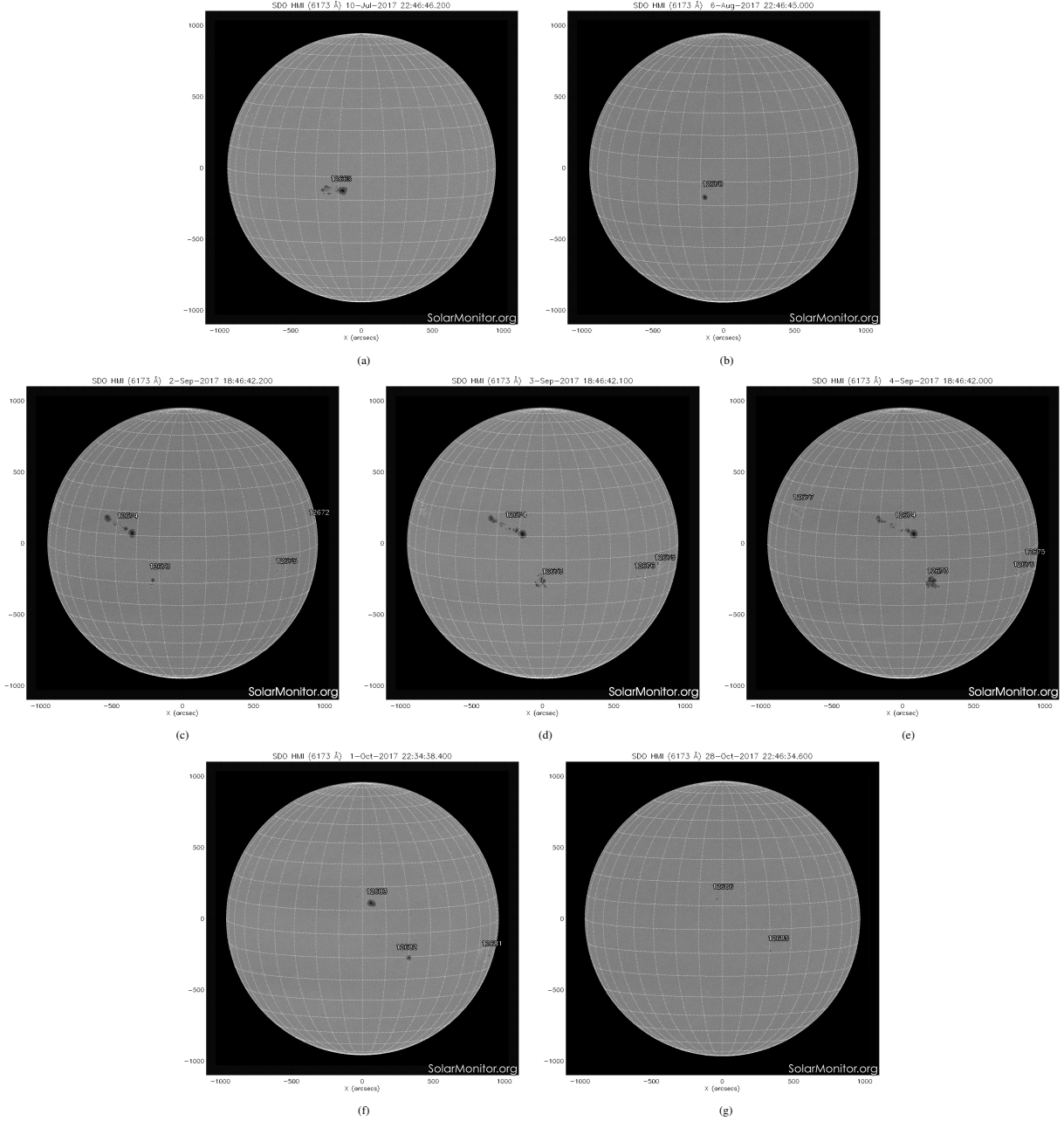


Figure 1. Prehistory, history, and posthistory of AR 12673 (full-disk photospheric images from <https://solarmonitor.org>): (a) sunspot group in AR 12665; (b) sunspot in AR 12670 at a time of one synodic rotation after (a); (c–e) sunspot pattern including a group in AR 12673 at three times taken 1 day apart, starting from a time of one synodic rotation after (b); (f) sunspot pattern including a spot in AR 12682 at a time of one synodic rotation after (e); (g) sunspot pattern including a spot in AR 12685 at a time of one synodic rotation after (f)

2. OBSERVATIONS AND DATA PROCESSING

Our study is based on data from the Helioseismic and Magnetic Imager (HMI) of the *Solar Dynamics Observatory* (SDO), which are stored at and available from the Joint Science Operations Center (JSOC, <http://jsoc.stanford.edu>). Specifically, we use a Spaceweather HMI Active Region Patch (SHARP; see [Bobra et al. 2014](#)) with the data remapped to a heliographic Lambert cylindrical equal-area projection (CEA). This automatically selected patch is cen-

tered at the flux-weighted centroid of the AR. The magnetic-field vector in the SHARP is decomposed into a radial (vertical), latitudinal and longitudinal components. The Dopplergrams are also CEA-remapped but not projected, still representing the line-of-sight, rather than radial, velocity component. We neglect the projection effects taking advantage of the fact that the AR was not far from the disk center on September 2–4, and the difference between the line-of-sight and the radial (vertical) component was not important.

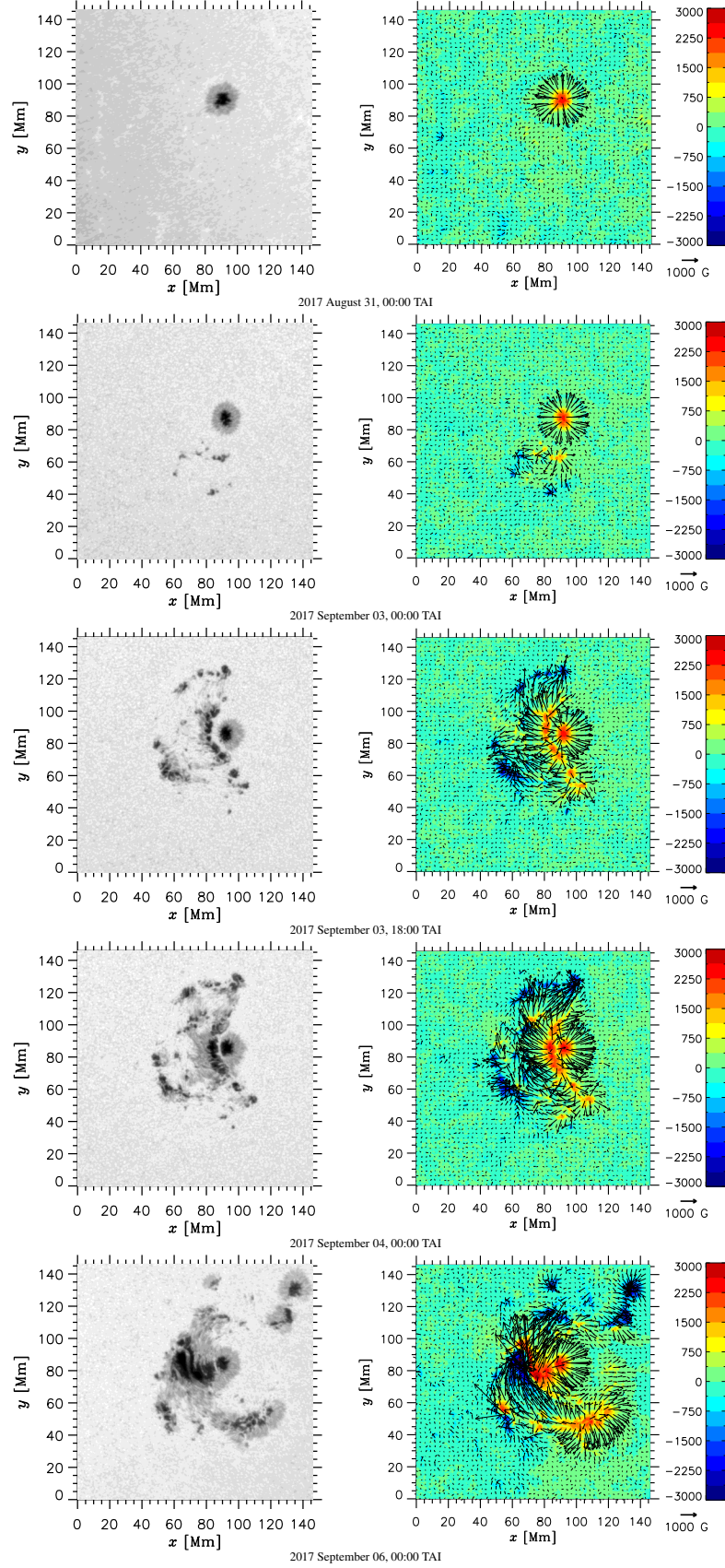


Figure 2. Pattern of AR 12673 in the Carrington frame of reference at five times, not equally spaced (indicated under each row of panels). Left: optical images; right: magnetic field (colors representing the vertical component in gauss and arrows representing the horizontal component)

As can be found from the headers of the downloaded FITS data files, the Carrington longitude of the center of this patch changed by 2.8 heliographic degrees over the 8-day period considered (2017 August 31, 00:00 TAI–2017 September 8, 00:00 TAI), the latitude being naturally constant. Alternatively to the SHARPs, JSOC offers a possibility of selecting, for a given AR, CEA-remapped arbitrarily-sized continuum-intensity image patches with a fixed Carrington longitude; such images can be downloaded with time cadences down to 45 s—in contrast to the SHARPs, which have a cadence of 12 minutes. We use the short-cadence patches to construct full-vector velocity maps with the horizontal velocities computed by a modified local-correlation-tracking (LCT) technique (Getling & Buchnev 2010). To jointly analyze the two sets of images, we cut out fragments coaligned with the short-cadence patches from the SHARPs, using the values of the Carrington longitude indicated in the FITS headers.

The pixel size of the HMI images is $0.5 \text{ arcsec} \approx 366 \text{ km}$. The SHARP under study originally measures 547×372 pixels, or $200 \times 136 \text{ Mm}^2$, and the size of short-cadence patches is 400×400 pixels, or $146.4 \times 146.4 \text{ Mm}^2$.

We apply Fourier subsonic filtering (Title et al. 1989) with a cutoff phase speed of 4 km s^{-1} to the continuum images and Dopplergrams taken with a cadence of 45 s. To eliminate the velocity fluctuations on a granular scale, we smooth the line-of-sight velocities and reduce each smoothed Dopplergram to zero average.

The LCT procedure is applied here to a sequence of images selected with a cadence of 135 s. For this procedure to be successful, we magnify the images doubling the number of pixels in each horizontal dimension with the use of a standard bilinear-interpolation procedure. To obtain final representations of the horizontal-velocity field, we either average the measured velocities over nine time steps (20 minutes 15 s), which yields vector velocity maps, or integrate the displacements of imaginary corks, or test particles, distributed over the area of interest, thus constructing cork trajectories for 2-hour time intervals.

We will be interested in assessing the proper motions of the two components of the AR. However, the motion of cluster (2), consisting of a multitude of small features, can hardly be inferred from the LCT-based velocity field, which gives an idea of the local flow structure but does not yield the bulk velocity of the cluster. This is why, along with employing the LCT technique, we estimate horizontal photospheric velocities by tracking the motion of some clear-cut features in the images, such as pores, umbral islands, and penumbral fragments. To this end, we visually identify these in a sequence of images and read their coordinates. The advantage of this approach stems from the possibility of choosing most representative markers of plasma motion and obtaining results less affected by (convective) noises.

3. EVOLUTION OF THE ACTIVE REGION

Figure 2 gives an overview of the evolution of AR 12673 as seen in white-light images and in magnetic-field vector maps (note that the both are not equally spaced in time). The coordinates x and y are measured in the longitudinal and the latitudinal direction, respectively. During the first two days after 2017 August 31, 00:00 TAI, the starting point of our consideration, the AR is represented in essence by only one isolated, well-developed positive-polarity sunspot (which has apparently survived two solar rotations that have elapsed after the decay of AR 12665); remember that we denote it as component (1) of the AR. It has a fairly regular structure with a nearly axisymmetric magnetic field, which exceeds 2300 G at the spot center (see the upper panel of Figure 2). In the Carrington frame of reference, the spot shifts eastward. It is remarkable in terms of its stability: it largely preserves its structure even at the later stage of strong interaction with cluster (2) consisting of smaller, less regular features.

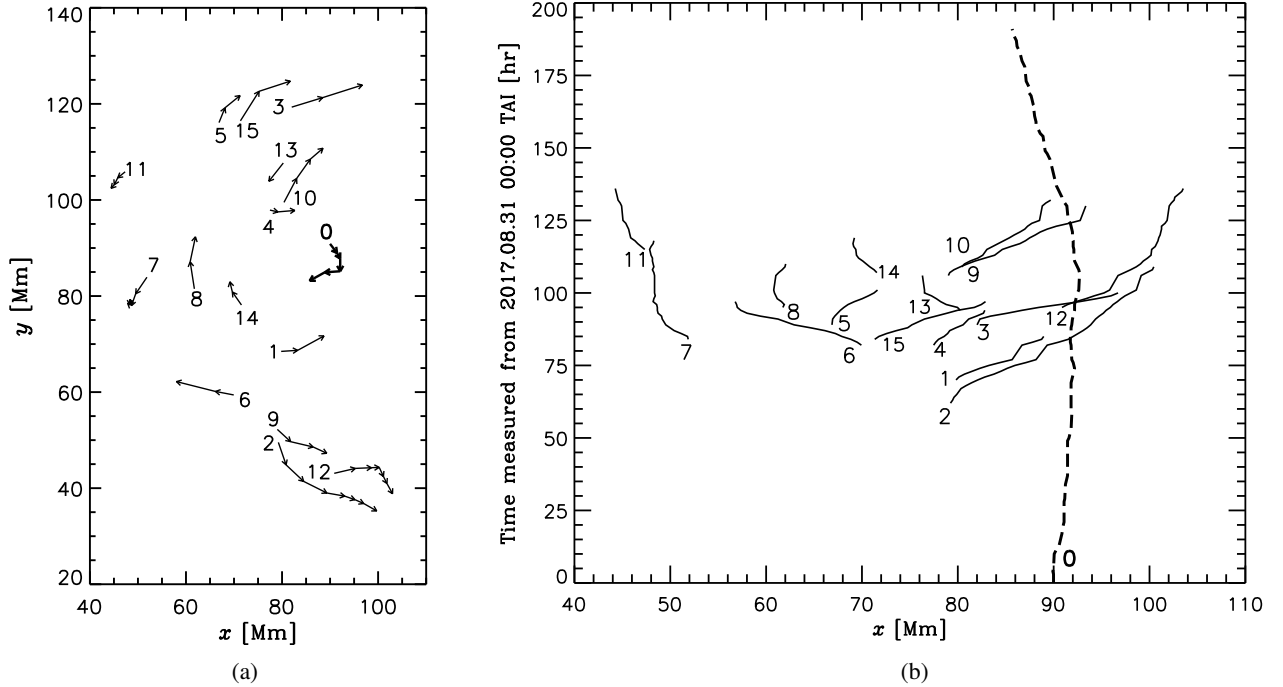
On September 2, cluster (2) starts developing south-southeast of sunspot (1). A multipolar magnetic pattern emerges together with small spots, pores, and fragments of penumbra (panel for September 3, 00:00, in Figure 2). During September 3, the cluster extends both longitudinally and especially latitudinally, acquiring a specific arcuate structure. Two elongated, bow-shaped chains of spot elements skirting around the major sunspot (1) originate, with two chains of magnetic elements spatially coinciding with them. The western chain is of the positive polarity, and the eastern one, of the negative polarity (see panel for September 3, 18:00). We will designate this evolutionary stage as the *two-arc stage*. These features persist over a certain time interval, the magnetic field being enhanced but the whole pattern experiencing only moderate complications in its structure (see panel for September 4, 00:00). At later times, the interaction between AR components (1) and (2) becomes so strong that the pattern of sunspots and magnetic field undergoes dramatic changes (panel for September 6, 00:00). It is worth noting that the first flare in this AR occurred near the end of the two-arc stage (on September 3, at 20:45), while all other flares took place after a significant complication of the magnetic field, starting from September 4, 22:10.

It is the two-arc stage of the evolutionary scenario that will be of particular interest to us. Before and during this stage, the pattern of sunspots and magnetic field remains relatively ordered and can give some insight into the underlying physical mechanisms.

Even a visual inspection of the panels of Figure 2 for September 3, 18:00, and September 4, 00:00, reveals that AR components (1) and (2) are in relative motion, coming close to each other. To quantify this motion, let us keep track of some features identifiable with most certainty in the optical images of the AR. Information on these features is

Table 1. Summary of the features tracked

Feature no.	t_{start} (hr)	t_{fin} (hr)	x_{start} (Mm)	x_{fin} (Mm)	y_{start} (Mm)	y_{fin} (Mm)	$\Delta x/\Delta t$ (Mm hr ⁻¹)
0	0	191	90.0	85.6	91.1	83.0	-0.023
1	70	85	79.4	89.6	68.8	72.8	0.68
2	62	109	79.4	101.0	50.1	33.7	0.46
3	89	100	80.5	98.0	118.9	124.0	1.59
4	82	94	76.8	83.4	97.7	98.8	0.55
5	89	101	66.2	72.1	114.9	122.2	0.49
6	82	97	70.6	57.1	60.0	61.5	-0.90
7	84	118	53.4	48.7	84.5	79.0	-0.14
8	95	110	62.6	62.2	80.1	93.6	-0.027
9	106	130	78.6	94.7	53.0	45.7	0.67
10	109	132	79.4	89.6	98.4	109.4	0.44
11	115	136	47.6	44.3	105.7	102.1	-0.16
12	95	136	90.0	104.3	42.4	36.9	0.35
13	94	106	80.8	75.0	107.9	104.3	-0.48
14	107	119	72.1	69.1	77.5	81.2	-0.25
15	84	97	70.6	83.8	114.5	125.5	1.02
Average of positive x -velocity values:							0.69 ± 0.27
Average of negative x -velocity values (feature 0 excluded):							-0.33 ± 0.24
Average of all x -velocity values (feature 0 excluded):							0.29 ± 0.49

**Figure 3.** (a) Map of drifting-feature tracks in the longitude–latitude plane; (b) longitude–time diagram of the drift of features

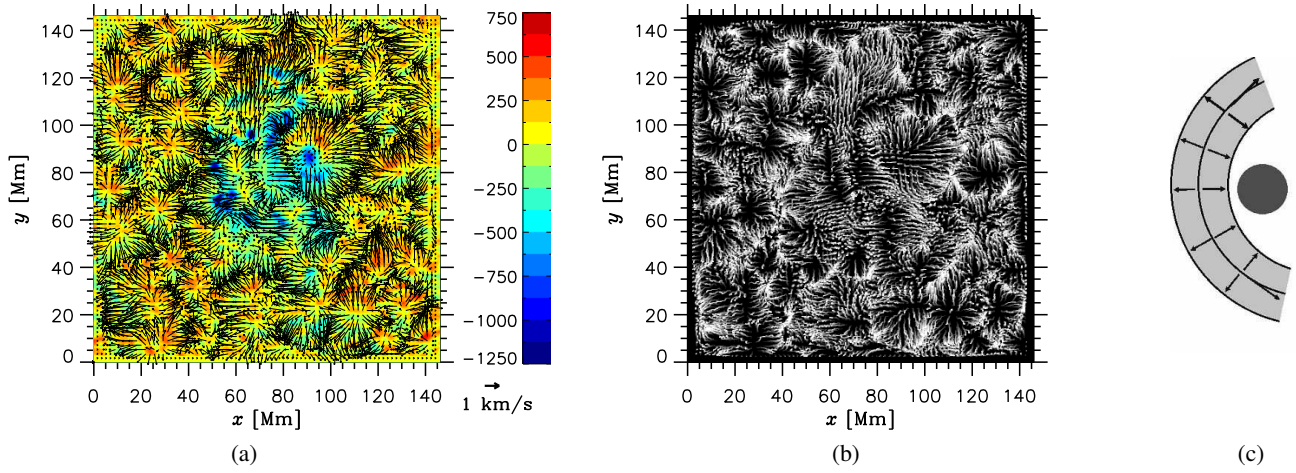


Figure 4. (a) Velocity field in AR 12673 at 2017 September 3, 13:22 TAI (colors representing the vertical velocity component in m s^{-1} and arrows representing the horizontal velocity component averaged over an interval of 20 minutes 15 s centered at that time; the scale of the horizontal velocity is shown with a heavy horizontal arrow at the bottom right of the figure); (b) map of cork trajectories obtained by integrating the cork displacements over an interval of 2 hr 17 minutes centered near that time (the initial point of each trajectory is black and the final point is white, the brightness gradually increasing with time); (c) schematic representation of the AR at the stage of the well-developed flow: the gray circle depicts the main sunspot with its magnetic field and the light-gray arcs show a simplified reconstruction of the overall geometry of the roll-type flow (arrows) with a velocity component along the rolls

summarized in Table 1; for each feature, it presents the initial, t_{start} , and the final, t_{fin} , time of the interval for which the feature was tracked (in hours, measured from August 31, 00:00), the initial $(x_{\text{start}}, y_{\text{start}})$ and the final $(x_{\text{fin}}, y_{\text{fin}})$ local coordinates of the feature (in Mm) in the short-cadence patches (fixed to the Carrington frame of reference), and the mean x -velocity of the feature (in Mm hr^{-1}) defined as $\Delta x / \Delta t$, where $\Delta x = x_{\text{fin}} - x_{\text{start}}$ and $\Delta y = t_{\text{fin}} - t_{\text{start}}$. The movements of these features are also shown by Figure 3a in the form of tracks on the longitude–latitude plane in the Carrington frame of reference and by Figure 3b in a longitude–time diagram, with each track labeled by the feature number in both panels.

Feature 0 is the main sunspot, or component (1) of the AR. Its track is shown by a heavy curve both in Figure 3a and Figure 3b. This spot exhibits only a moderate shift in the Carrington frame of reference with a mean x -velocity of about $-0.023 \text{ Mm hr}^{-1}$. The tracks of other features mainly refer to the two-arc stage and to the stage of subsequent complication of the entire pattern, September 3 and 4 (times of 72–120 hr). What attracts one’s attention in Figure 3b is the fact that most features in the right-hand part of the diagram (region $x > 65 \text{ Mm}$) move westward, while a few features (6, 7, 11, 13, 14) in its left-hand part exhibit eastward drift. The entire flow pattern appears more consistent as considered in the longitude–latitude plane (Figure 3a). It becomes clear that these movements are predominantly directed along the arcs, roughly, to the northwest in the northern part of the pattern and to the southwest in its southern part (more precisely, the separatrix between the northward and southward streams is directed to the southeast of the main spot). Very few features exhibit arc-aligned movements directed oppositely compared

to nearby features, so that countercurrent streams are intermixed to a certain extent: feature 13 moves oppositely compared to nearby features 3, 5, 10, 15, and features 7 and 11 move oppositely compared to feature 8. There are also motions across the arcs (features 1, 4, 6). They can be revealed more clearly from velocity maps; we will discuss them below.

While feature 0 (the main sunspot) slightly shifts eastward, the cluster comprising other features moves as a whole westward, as can be grasped from Figure 3. This is apparent despite the presence of inner motions superposed on the bulk motion of the cluster. The data presented in Table 1 and visualized in Figure 3 make it possible to estimate the relative velocity of spot (1) and cluster (2). Comparatively stable and well localized features are few in number, and averaging their velocities implies fairly large mean absolute deviations (they are indicated in the table). Nevertheless, a figure of order 0.3 Mm hr^{-1} seems to be a realistic estimate for the westward velocity of the cluster relative to the Carrington frame of reference and to the main spot.

On the whole, as Figure 3a demonstrates, the pattern of motion of the features about the main spot bears amazing resemblance to the pattern of a *fluid flow about a roundish body*. At the same time, the pattern of local inner motions in cluster (2), as obtained using the LCT technique, exhibits some likeness to the pattern of roll thermal convection. This is most pronounced at the two-arc stage of AR development and illustrated in Figure 4a by a full-vector map and in Figure 4b by a map of cork trajectories: the flow pattern is like that of two bowed convection rolls with superposed arc-aligned motions, as crudely sketched in Figure 4c (where the

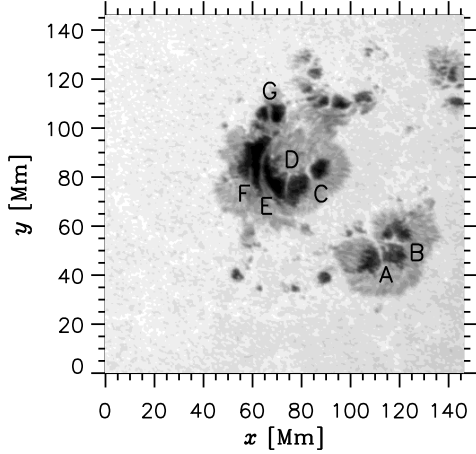


Figure 5. Optical image of AR 12673 for 2017 September 07, 05:00 TAI, with several light bridges (labeled with letters) intersecting the umbrae of sunspots

arrows only indicate the preferred flow directions rather than represent local velocity vectors).

The indications for a roll flow are not very surprising by themselves: roll-like motions were previously detected in the solar photosphere (Getling 2006; Getling & Buchnev 2008). In our case, it is remarkable that (i) roll motions can be detected in the area where a relatively strong magnetic field with a fairly complex structure is present and (ii) the roll-flow pattern interacts with an obstacle moving relative to this pattern, i.e., with the coherent magnetic field of the main sunspot, and experiences deformations due to this interaction. Fine details complicating the pattern seemingly reflect a considerable role of the magnetic field affecting the flow.

4. PHYSICAL INTERPRETATION

Our interpretation of the above-described evolution pattern of AR 12673 is based on the available information on the differential rotation of the Sun. We use data of helioseismological inversions determining the rotation rate of deeper layers. In particular, the difference in the rotation rate across the near-surface shear layer, or leptocline, can be estimated based on Figure 1 of Howe et al. (2000). Specifically, at a latitude of $\varphi = \pm 9^\circ$, nearly corresponding to the latitude of AR 12673, the rotation rate $\Omega/2\pi$ increases from the surface to depths of about $0.04R_\odot$ by $\Delta\Omega/2\pi \approx 15$ nHz (having characteristic values of about 460 nHz). The corresponding linear-velocity shear in a solidly rotating frame of reference is $\Delta v = \Delta\Omega R_\odot \cos \varphi = 0.233$ Mm hr⁻¹, which is a quantity of the same order of magnitude as the relative velocity of the main sunspot (1) and cluster (2), 0.3 Mm hr⁻¹. More precisely, such a velocity increase, Δv , should be achieved at depths of about $0.03R_\odot$. This suggests that *the main sunspot may be dynamically coupled to higher layers than the cluster*. The well-developed, stable magnetic feature—sunspot (1)—

extends through the leptocline but moves with the surface layers, while the plasma of the deeper layers flows about this magnetic obstacle together with cluster (2). The long prehistory of sunspot (1) may be fair indication that it has had time to become “fixed” to near-photospheric layers, whereas the fresh cluster magnetic field developing at deeper levels has not.

We can also put forward some tentative considerations of the magnetic-field emergence in cluster (2) during the two-arc stage. The observed pattern of this process resembles the interaction of two convection rolls with a horizontal magnetic sheet lying at a certain depth. The field in this sheet should be directed from west to east. As it is carried by the upflow extending along the join between the two convection rolls and then stretched by the diverging eastward and westward flows, it can form the negative and the positive arc observed along the downflow portions of the rolls.

5. NOTES ON THE FORMATION OF LIGHT BRIDGES

In addition, an interesting comment can be made on the formation process of light bridges in sunspot umbrae. This phenomenon is typically attributed to the decay stage of sunspots (see, e.g., Felipe et al. 2016, where a comprehensive survey of light-bridge properties is in particular given). AR 12673, which we consider here, demonstrates a different scenario of the development of light bridges.

The last three rows of Figure 2 show the merger of cluster (2) with spot (1) giving rise to a larger sunspot with a more complex structure and the development of a new sunspot from cluster (2) in the southwestern part of the AR via aggregation of small umbral and penumbral fragments. An even later stage of the process is illustrated by Figure 5, which refers to a time when the formation of both the complex sunspot and the new one has been basically completed. It can be seen that a number of light bridges are present in the two spots.

Among them, bridge C was formed first. This occurred as spot (1) and well-developed cluster (2) came close together to form a complex sunspot with a few umbral areas and a common penumbra, the bridge appearing as a remnant of the bright space that had previously separated the two components of the AR. A similar merger of fragments of cluster (2) gave rise to bridges A and B in the newly formed southwestern sunspot. Thus, the formation of light bridges A–C is not related to the decay of sunspots. These bridges can be classified as *strong* light bridges (see Felipe et al. 2016): the magnetic field on both sides of them has the same polarity.

The other bridges were formed differently. Bridges E, F and G resulted from the proximity of dark and light features moving about sunspot (1) in different directions (as features 8 and 14 compared to 7, 11, and 9 do in Figure 3a) and producing a shear flow. Lastly, bridge D originated from the penetration of a penumbral area into an umbra; in essence,

only its origin can be associated with the disintegration of a sunspot.

6. SUMMARY AND CONCLUSION

We have analyzed the dynamics of AR 12673 using *SDO/HMI* data for 2017 August 31, 00:00 TAI–2017 September 8, 00:00 TAI. The sunspot group in this AR consisted of (1) an old, well-developed and highly stable, coherent sunspot and (2) a rapidly developing cluster of umbral and penumbral fragments. The most remarkable manifestation of the cluster evolution is the formation of two elongated, arcuate chains of spot elements skirting around the major sunspot (1), with two chains of magnetic elements spatially coinciding with the arcs (the two-arc evolutionary stage). The western chain is of the positive polarity, and the eastern one, of the negative polarity. Components (1) and (2) are in relative motion, coming close to each other, with cluster (2) overtaking spot (1) at a speed of order 0.3 Mm hr^{-1} .

On the whole, the pattern of motion of the features about the main spot bears amazing resemblance to the pattern of a fluid flow about a roundish body. Together with the estimate of the relative speed of components (1) and (2) and in view of the existence of a near-surface shear layer, or leptocline, this suggests that the main spot may be dynamically coupled to higher layers than the cluster. According to helioseismological data, at the latitude of AR 12673, in a solidly rotating frame of reference, the linear velocity shear between the photosphere and the base of the leptocline (a depth of $0.04R_{\odot}$) is 0.233 Mm hr^{-1} . The estimated relative speed of sunspot (1) and cluster (2) should therefore be achieved at depths of about $0.03R_{\odot}$. Likely, the well-developed, stable magnetic feature—sunspot (1)—extends through the leptocline but moves with the surface layers, while the plasma

of the deeper layers flows about this magnetic obstacle together with cluster (2). The long prehistory of spot (1) may be fair indication that it has had time to become “fixed” to near-photospheric layers, whereas the fresh cluster magnetic field developing at deeper levels has not. It seems reasonable to find out in further studies whether relatively low revolution rates is a distinctive property of old, stable sunspots.

The pattern of local inner motions in cluster (2) exhibits some likeness to the pattern of roll thermal convection. The observed pattern of magnetic-field emergence in cluster (2) during the two-arc evolutionary stage resembles the interaction of two convection rolls with a horizontal magnetic sheet lying at a certain depth.

During the evolution of AR 12673, a few light bridges develop in the sunspot group. The formation of some of them is definitely not related to the decay of sunspots; in contrast, they are remnants of the bright space between the spots that have come close to each other. These bridges can be classified as strong light bridges: the magnetic field on both sides of them has the same polarity. The development of only one bridge can be associated with the disintegration of a sunspot.

We see that the pattern of relative motion of different photospheric features may prove to be informative about the interaction of different near-photospheric layers. The diagnostic value of the flow patterns seems to deserve further investigation, in particular, with invoking helioseismological data.

The observational data were used here by courtesy of NASA/SDO and the HMI science teams. I am grateful to A. A. Buchnev, who developed the modified-LCT and the cork-tracking procedure, and to B. Yu. Yushkov for a useful comment.

REFERENCES

- Attie, R., Kirk, M. S., Thompson, B. J., Muglach, K., & Norton, A. A. 2018, *Space Weather*, 16, 1143, doi: [10.1029/2018SW001939](https://doi.org/10.1029/2018SW001939)
- Bobra, M. G., Sun, X., Hoeksema, J. T., et al. 2014, *SoPh*, 289, 3549, doi: [10.1007/s11207-014-0529-3](https://doi.org/10.1007/s11207-014-0529-3)
- Felipe, T., Collados, M., Khomenko, E., et al. 2016, *A&A*, 596, A59, doi: [10.1051/0004-6361/201629586](https://doi.org/10.1051/0004-6361/201629586)
- Getling, A. V. 2006, *SoPh*, 239, 93, doi: [10.1007/s11207-006-0231-1](https://doi.org/10.1007/s11207-006-0231-1)
- Getling, A. V., & Buchnev, A. A. 2008, *SoPh*, 248, 233, doi: [10.1007/s11207-007-9056-9](https://doi.org/10.1007/s11207-007-9056-9)
- . 2010, *Astron. Rep.*, 54, 254, doi: [10.1134/S1063772910030078](https://doi.org/10.1134/S1063772910030078)
- . 2019, *ApJ*, 871, 224, doi: [10.3847/1538-4357/aafad9](https://doi.org/10.3847/1538-4357/aafad9)
- Hou, Y. J., Zhang, J., Li, T., Yang, S. H., & Li, X. H. 2018, *A&A*, 619, A100, doi: [10.1051/0004-6361/201732530](https://doi.org/10.1051/0004-6361/201732530)
- Howe, R., Christensen-Dalsgaard, J., Hill, F., et al. 2000, *Science*, 287, 2456, doi: [10.1126/science.287.5462.2456](https://doi.org/10.1126/science.287.5462.2456)
- Sun, X., & Norton, A. A. 2017, *Research Notes of the American Astronomical Society*, 1, 24, doi: [10.3847/2515-5172/aa9be9](https://doi.org/10.3847/2515-5172/aa9be9)
- Title, A. M., Tarbell, T. D., Topka, K. P., et al. 1989, *ApJ*, 336, 475, doi: [10.1086/167026](https://doi.org/10.1086/167026)
- Yang, S., Zhang, J., Zhu, X., & Song, Q. 2017, *ApJL*, 849, L21, doi: [10.3847/2041-8213/aa9476](https://doi.org/10.3847/2041-8213/aa9476)